Simulating the effect of high-intensity sound on cetaceans: Modeling approach and a case study for Cuvier's beaked whale (*Ziphius cavirostris*)

P. Krysl[a)]
University of California, San Diego, 9500 Gilman Drive No. 0085, La Jolla, California 92093-0085

T. W. Cranford
San Diego State University, 5500 Campanile Drive, San Diego, California 92182

S. M. Wiggins and J. A. Hildebrand
Scripps Institution of Oceanography, University of California, San Diego, 9500 Gilman Drive, No. 0205, La Jolla, California 92093-0205

(Received 23 December 2005; revised 16 June 2006; accepted 29 June 2006)

A finite element model is formulated to study the steady-state vibration response of the anatomy of a whale (Cetacea) submerged in seawater. The anatomy was reconstructed from a combination of two-dimensional (2D) computed tomography (CT) scan images, identification of Hounsfield units with tissue types, and mapping of mechanical properties. A partial differential equation model describes the motion of the tissues within a Lagrangean framework. The computational model was applied to the study of the response of the tissues within the head of a neonate Cuvier's beaked whale *Ziphius cavirostris*. The characteristics of the sound stimulus was a continuous wave excitation at 3500 Hz and 180 dB re: 1 μPa received level, incident as a plane wave. We model the beaked whale tissues embedded within a volume of seawater. To account for the finite dimensions of the computational volume, we increased the damping for viscous shear stresses within the water volume, in an attempt to reduce the contribution of waves reflected from the boundaries of the computational box. The mechanical response of the tissues was simulated including: strain amplitude; dissipated power; and pressure. The tissues are not likely to suffer direct mechanical or thermal damage, within the range of parameters tested. © *2006 Acoustical Society of America.*
[DOI: 10.1121/1.2257988]

PACS number(s): 43.80.Gx, 43.80.Nd, 43.80.Lb, 43.80.Jz [WWA] Pages: 2328–2339

I. INTRODUCTION

Recently, attention has been directed toward understanding the relationship between cetacean stranding and high-intensity sound, particularly the potential for midfrequency naval sonar to cause stranding of beaked whales (Frantzis, 1998; NOAA, 2001; Balcomb and Claridge, 2003; Hildebrand, 2005). The overall pattern of these strandings has raised concerns that sounds from sonar could directly or indirectly result in the death or injury of beaked whales, particularly Cuvier's beaked whale (*Ziphius cavirostris*). The connection between sound exposure and cetacean stranding is not yet understood in terms of physiological or behavioral responses to sound (Cox *et al.*, in press; Rommel *et al.*, in press). To address some of these issues we present an investigation of the direct impacts of sound on beaked whale head tissues, presumed to be the most susceptible to anthropogenic sound impact.

We aim to develop techniques to model how high-intensity underwater sound interacts with cetacean anatomy and physiology. In this study, we first evaluate how well modern finite element modeling tools are capable of simulating the interaction between anatomic geometry, tissue properties, and sound sources with various characteristics. Then we model the interactions between sound waves and anatomy within the head of a specimen of Cuvier's beaked whale (*Ziphius cavirostris*). We chose this species because it has stranded in the greatest numbers during incidents associated with exposure to midfrequency sonar (Cox *et al.*, in press). The specimen of *Ziphius cavirostris* modeled in this study was the subject of computed tomography (CT) scans and tissue property measurements reported elsewhere (Soldevilla *et al.*, 2005). Consequently, more is known about the anatomy and physical properties of this specimen than any other single beaked whale.

In conjunction with our primary objective of developing modeling tools for the study of cetaceans, we investigated whether sounds with characteristics similar to those used in midfrequency naval sonar are capable of producing direct effects on cetacean tissues. We seek to understand whether vibrations of high-displacement amplitude or high-strain amplitude could lead to large amounts of energy being dissipated in the soft tissues causing thermal damage. Our model is formulated as follows. Consider an animal submerged in seawater; the animal's head is exposed to sound excitation which arrives in the form of continuous planar sound waves of a given frequency, direction, and sound pressure level.

[a)]Electroni mail: pkrysl@ucsd.edu

 0001-4966/2006/120(4)/2328/12/$22.50

We simulated the steady state vibration response of the tissues and assessed the quantitative mechanical characteristics of such motion.

Modeling sound propagation using numerical methods has been used previously to investigate sound generation and propagation pathways in a dolphin's head. Aroyan *et al.* (1992) used a two-dimensional numerical model to test ideas about dolphin sonar signal generation and emission (Cranford, 1988). Aroyan (2001) evaluated the competing and prevailing hypotheses for sonar signal transmission and reception (Norris, 1964; Brill and Harder, 1991; Cranford *et al.*, 1996) by creating a simulated three-dimensional acoustic propagation model. Primarily, these studies demonstrated the promise of using numerical methods to query anatomic systems about acoustic questions. One drawback in the studies of Aroyan and colleagues is that they used a simplified estimate of tissue properties. They assumed that tissues behave like fluids and did not consider the complex interactions between the solid properties of tissues and organs. The combination of techniques developed for the current study provides a more realistic approximation of tissue properties than that used by previous authors.

Finite element modeling (FEM) has become an established tool for an ever-widening sphere of applications. For instance, it has long been used by engineers to simulate the effects of vibrations on structures like buildings, bridges, and machines. Nowadays it is also being increasingly used to study the effects of stress/strain regimes on biological structures. The formulation of a biomechanical model involves a number of factors, including: the geometrical complexity of the anatomy; the heterogeneity, anisotropy, and rate-dependent response of the tissues; and computational costs. Also, the infinite extent modeling of the surrounding media (water) must be considered, since the sound waves that impinge upon the animal are reflected and scattered and propagate away in all directions, as well as being transmitted into the tissues.

This paper opens with a brief recapitulation of the partial differential equations that describe a model for deformations of tissues due to acoustic vibrations. It proceeds with a discussion of a constitutive equation, and formulates a strategy for the treatment of boundary conditions and a description of finite element discretization. The paper concludes with a case study, in which the modeling approach is used to assess the effects of selected high-intensity sound on the head anatomy of a neonate Cuvier's beaked whale *Ziphius cavirostris*.

II. MODEL

We present a brief description of the adopted partial differential equation (PDE) model that is used to describe the motion of the soft and hard tissues (and the surrounding water), both during the steady state forced vibration produced by progressive sound waves, and during any transient vibrations.

A. Governing equations

We consider the model of small-strain and small-displacement deformation of continuous media. Even for sound pressure levels ~200 dB, we would not expect the amplitude of the displacements to be larger than a few dozen micrometers and our results for the case study confirm this. A strictly Lagrangean description is adopted, for both solids and fluids (i.e., the particles of the continuum are tracked in time, as opposed to the Eulerian approach in which the continuum is watched as it flows through a control volume fixed in space). The continuum occupies volume V, whose bounding surface is S, and the time-dependent deformation is followed in the interval $0 \le t \le t_{\text{final}}$. The vector of engineering strains $\varepsilon = \{\varepsilon_{xx}, \varepsilon_{yy}, \varepsilon_{zz}, \gamma_{xy}, \gamma_{xz}, \gamma_{yz}\}^T$ (the superscript T indicates transpose) is defined as

$$\varepsilon = Bu,$$

where $u = \{u_x, u_y, u_z\}^T$ is the displacement vector, and

$$B = \begin{bmatrix} \partial/\partial x & & \\ & \partial/\partial y & \\ & & \partial/\partial z \\ \partial/\partial y & \partial/\partial x & \\ \partial/\partial z & & \partial/\partial x \\ & \partial/\partial z & \partial/\partial y \end{bmatrix},$$

is the symmetric gradient matrix operator. The balance equation is

$$\rho \ddot{u} = B^T \sigma,$$

where ρ is the mass density, $\sigma = \{\sigma_{xx}, \sigma_{yy}, \sigma_{zz}, \sigma_{xy}, \sigma_{xz}, \sigma_{yz}\}^T$ is the stress vector, and $\ddot{u}$ is the second order time derivative of the displacement vector. Note that body forces are omitted in the balance equation. The constitutive equation is in general a relationship between stress and the independent variables strain and strain rate

$$\sigma = \sigma(\varepsilon, \dot{\varepsilon}).$$

The boundary conditions on $y \in S$ are written for the traction vector

$$(P_n \sigma)_i = \bar{t}_i,$$

where

$$P_n = \begin{bmatrix} n_x & & & n_y & n_z & \\ & n_y & & n_x & & n_z \\ & & n_z & & n_x & n_y \end{bmatrix}$$

is the projector on to the direction of the outer normal n, and $\bar{t}_i$ is the prescribed value of the traction component. For the velocity vector boundary conditions, where $\bar{v}_i$ is the prescribed velocity component

$$\dot{u}_i = \bar{v}_i.$$

Likewise, the initial conditions are

$$\dot{u}(x, t=0) = \bar{v}(x),$$

and

$$\sigma(x, t=0) = \bar{\sigma}(x).$$

B. Constitutive equation for soft tissue

To complete our model for time-dependent deformation of soft tissue, we need a constitutive equation with estimates for the associated material constants. Several good models of dissipative behavior of soft tissues exist, for instance, Rubin and Bodner (2002). However, for a given class of tissue, many material parameters are required, few of which have been thoroughly measured. Soldevilla *et al.* (2005) recently characterized the soft tissues of a neonate beaked whale (the same specimen used in our study), providing a map from CT scan data of x-ray attenuation Hounsfield units to mass density, dilatational sound speed, and the Young's modulus. Based on Soldevilla *et al.* (2005) results, the tissue properties are assumed to be isotropic, making, it is possible to extract from these experiments a full set of material parameters for the classical PDE of inhomogeneous isotropic elastodynamics. Therefore, as a first step we propose to use the constitutive model of isotropic viscoelastic response

$$\sigma = Kmm^T\varepsilon + 2GI_0I_d\varepsilon + 2\eta I_0I_d\dot{\varepsilon},$$

where K is the bulk modulus, G is the shear modulus, η is the dynamic viscosity, $m=[1,1,1,0,0,0]^T$, $I_0 = \frac{1}{2}\,\mathrm{diag}([2,2,2,1,1,1])$, $I_d=I-\frac{1}{3}mm^T$ is the deviatoric projector, I is the identity, and $\dot{\varepsilon}$ is the strain rate vector. Note that bulk viscosity has been omitted because it is generally considered less important at lower frequencies than shear viscosity (it is two or more orders of magnitude smaller; in addition, the dilatational strain rate is typically much lower in magnitude than shear strain rate). The use of this constitutive equation (under the label "Voigt's model") recently has been justified in transient elastography of soft tissues by Catheline *et al.* (2004).

C. Solution strategy for a bounded volume

The intent is to obtain a solution to the above equations that represents a steady-state forced vibration produced as a response to the continuous sound excitation. The solutions to the above PDE model are both progressive and standing waves. It is reasonable to assume that the surrounding seawater is infinite in extent (i.e., the free surface is ignored). The computational domain could also be infinite, and there are several possible approaches to address this problem [refer for instance to the review by Astley (2000)]: boundary element methods; methods that combine finite and infinite elements; or methods that combine finite elements with boundary elements (Wagner, 2004). Alternatively, the domain may be truncated, with the infinite part replaced by appropriate boundary conditions applied to the finite part; for instance the nonreflecting boundary conditions of Bayliss *et al.* (1982), or the perfectly matched layer formulation of Festa and Vilotte (2005). As a matter of expediency, this study made use of the finite-domain discretization, while we are evaluating all of the mentioned approaches as a means of controlling the approximation error.

During steady-state vibration, the plane sound waves that impinge upon the tissues are converted into a mixture of dilatational pressure and shear waves. These waves are reflected from, and transmitted across any impedance-mismatch interface, in particular the interface between soft tissue and bone, and between soft tissue or bone and an airspace. Any waves that reflect off the anatomy and arrive at the boundary of the computational volume will be reflected back into the volume, unless we control for them, for instance, by using the perfectly matched layer (PML) approximation (Festa and Vilotte, 2005) which introduces an anisotropic lossy material along the boundary to absorb oncoming waves. Since PML approximations tend to be computationally expensive and complex, and since we are not interested in the propagation of the reflected waves through the surrounding water, we make the entire water volume into an absorbing layer by suitably increasing its (Newtonian) viscosity to damp shear deformations. It should be noted that the sound waves of the acoustic stimulus will also be damped since the rate of shearing is nonzero in the forcing planar wave. The deviatoric components of the reflected waves that have left the tissue sample and are propagating toward the boundary, or of the waves that have been reflected from the boundary, will be strongly damped. Clearly, this is an approximation in that the reflected dilatational waves are not being damped until they get converted fully or partially into motions with nonzero shear (rate) components.

With the described approximate treatment of the effect of the finite extent of the computational box, it is possible to formulate a solution strategy: given any consistent set of boundary and initial conditions, integrate the governing equations in time until a steady state is reached. The quantities of interest are then directly available in the solution data. This approach resembles the dynamic relaxation solution techniques applied to static problems (e.g. Řeřicha, 1986).

D. Finite element discretization

Standard Galerkin discretization of the weak form of the PDE model leads to a system of ordinary differential equations

$$M\ddot{U} = F,$$

where M is the time-independent mass matrix; $\ddot{U}$ is the vector of all free components of the displacement; and F is the vector of corresponding effective forces (external and internal). The discretization in time follows the classical Newmark (centered differences) template, from which we obtain the time stepping scheme

$$A^{(n)} = M^{-1}F^{(n)}$$

$$U^{(n+1)} = U^{(n)} + \Delta t V^{(n)} + \frac{\Delta t^2}{2}A^{(n)},$$

$$V^{(n+1)} = V^{(n)} + \frac{\Delta t}{2}(A^{(n-1)} + A^{(n)})$$

where $A^{(n)}, V^{(n)}$ are approximations to the second and first order derivative (acceleration and velocity) of the vector of unknown displacements $U^{(n)}$ and Δt is the time step. For the prescribed velocity degrees of freedom, $V_j^{(n)}=\bar{V}_j^{(n)}$, the first equation is replaced with $A_j^{(n)}=\frac{2}{\Delta t}(\bar{V}_j^{(n)}-V_j^{(n-1)})-A_j^{(n-1)}$. The

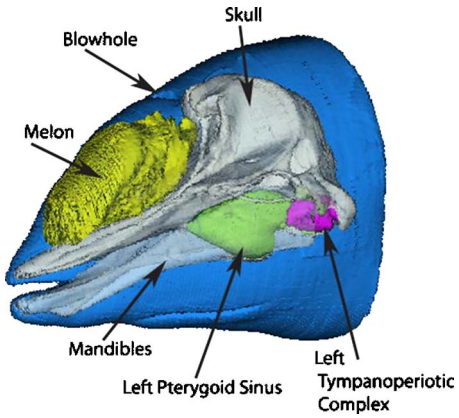

FIG. 1. (Color online) Left anterolateral view of the head of a female neonate Cuvier's beaked whale (*Ziphius cavirostris*). The image was reconstructed from CT scans by segmentation of the anatomical structures. The structural color scheme is as follows: skin=blue; skull=white; mandibles =light blue; melon=yellow; left pterygoid sinus=green; left tympanoperiotic complex=magenta.

initial values $U^{(0)}$ and $V^{(0)}$ (and also the initial stress) are determined by the initial conditions.

Hexahedral isoparametric eight-node brick elements are used throughout the mesh. The use of the simple isotropic constitutive equation allows us to formulate an effective computational procedure to deal with almost incompressible materials. In the materials that possess nonzero shear modulus (connective tissue, muscle, and fats) volumetric locking is mitigated by using the selective reduced integration procedure of Hughes (2000) (one-point integration of the volumetric response, and full $2\times2\times2$ quadrature of the shear terms). The volumetric term in the elements that represent water (zero elastic shear stiffness) are stabilized by mixing a very small fraction of fully integrated forces with the one-point-rule integrated response.

III. CASE STUDY—*Ziphius cavirostris*

The head of a neonate Cuvier's beaked whale (specimen NMFS field number KXD0019) *Ziphius cavirostris*, from which tissue properties were measured by Soldevilla *et al.* (2005), is examined in the present computational study (Fig. 1). We compute the mechanical response of the soft tissues of the head, including those associated with peripheral sound reception. The acoustic stimulus was a series of planar sound waves from the right side of the computational box with a given frequency (3500 Hz), and a given intensity (sound pressure level (SPL) =180 dB re 1 μPa). The characteristics of the acoustic stimulus roughly match estimates of potential maximum received sound pressure levels during exposure to mid-frequency sonar associated with the Bahamas beaked whale strandings (NOAA, 2001).

Several structures within the head of the neonate Cuvier's beaked whale (Fig. 1) are of interest in the production or reception of sound (Cranford and Amundin, 2003). Sound production is associated with air movement within a set of sacs located beneath the blowhole, between the melon and the skull. The melon is composed of fatty tissues and acts as an acoustic channel for sound propagating out of the head. The lower half of the head contains the mandibles, acoustic fats associated with sound reception, air-filled pterygoid sinus, and the bony ear (tympanoperiotic) complex. The juxtaposition of the air-filled sinus and the bony ear complex represents the greatest impedance mismatch within this animal.

To construct an anatomical model, the head of the neonate Cuvier's beaked whale was scanned with x-ray computed tomography (CT), as reported by Soldevilla *et al.* (2005). The data were collected continuously with 152 transverse scans along the longitudinal axis. Each of these transverse scans was 5 mm thick, collected every 5 mm. The GE Lightspeed scanner used a 500 mm diameter field of the view scan region and a scanning protocol as reported in Soldevilla *et al.* (2005). In addition to the anatomic data, tissue samples from the neonate Cuvier's beaked whale were studied for physical properties including density, sound velocity, and Young's modulus.

A. Data processing

The computational domain is a rectangular three-dimensional box representing a volume of water with the specimen inside. The dimensions of the computational box can be found in Fig. 2 (all dimensions in millimeters). The anatomy is defined by a three-dimensional array of voxels as generated by a CT scan (referred to hereafter as raw data). The voxel values are in the Hounsfield units that may be mapped to material density and other material parameters as described by Soldevilla *et al.* (2005). The matrix size is 512×512 pixels in each transverse or cross-sectional scanning plane. The resolution within each transverse plane is 1.5 mm square pixels.

The original CT data have been minimally processed to produce the input three-dimensional (3D) voxel array. All of the voxels external to the boundary of the head were converted to a Hounsfield value corresponding to seawater. Thus, the specimen is, in this simulation, immersed in an environment of sea water near sea-surface pressure. The addition of water outside the specimen ensures adequate space between the specimen and the bounding box for the simulations. In this study we provided a space of approximately 30 to 80 mm between the specimen and the bounding box.

Another adjustment to the CT data was applied to the air sinuses that occur normally within the head and air-filled voids created by the postmortem nature of the specimen. The pterygoid sinuses and any air-filled voids were assigned an artificial Hounsfield value of −2000 (a value not found in the original CT image data) so that these voxels could be recognized and dealt with appropriately during the mesh generation process. Consequently, we could fill in voids that are not normally present, for example, those left after blood drained from them. This step also provided a means to access these internal regions, separately or collectively, in order to test ideas of their effect on the system. No further editing of the CT data was undertaken for this study.

B. Generation of the finite element meshes

The input 3D voxel array was resampled using linear interpolation to produce voxels of desired resolution. The

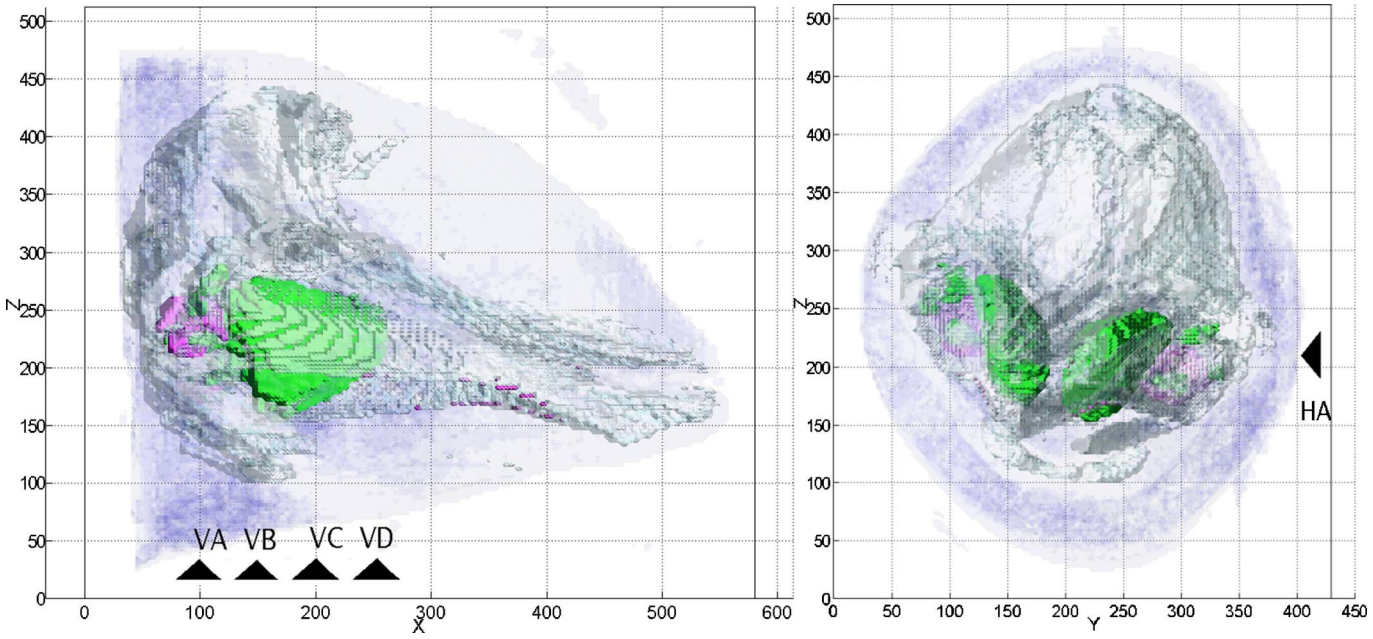

FIG. 2. (Color online) The head within the computational volume or "box." The frontal view is in the right panel, and right lateral view is in the left panel. The soft tissues are displayed with some transparency to reveal the internal structure, especially the pterygoid sinuses (air cavities) in green, and the high-density tympanoperiotic complexes (ear bones) in magenta. The horizontal slice location is indicated with "HA" in the right panel. The vertical slice locations (perpendicular to the longitudinal axis of the animal) are indicated with "VA," "VB," "VC," and "VD" in the left panel. The geometry is shown at the sample resolution corresponding to the finest mesh used in this paper $N=152$. Some visible artifacts appear, for instance the topographic curves along the surface of the mandible in the left panel.

voxels of the resampled array were then converted directly into finite elements, each of which was assigned a single material property based on the value of the x-ray attenuation Hounsfield unit in the voxel.

Four different meshes have been used, with N number of cells in the longitudinal direction $N \in \{80, 99, 123, 152\}$. Correspondingly, the total number of finite element nodes varied between 340,000 and 2.5 million, and the spatial resolution varied between 6.91 and 3.61 mm. The finite elements were nearly cubic. In the transverse plane the finite elements are lower resolution than is available from the original scan; in the longitudinal direction the resolution is comparable (5 mm in the scan compared to 6.91 to 3.61 mm for the finite elements).

C. Initial and boundary conditions

For simplicity, the computational box is assumed initially at rest, and unstressed. Such an assumption makes it easy to reconcile the boundary and the initial conditions. It also implies that the specimen and its bounding box are near the sea surface and that the system is not exposed to significant hydrostatic pressure. In this case, we used the geometry of the air sinuses as we found them. The geometry of air spaces, such as the pterygoids or peribullary sinuses (Fraser and Purves, 1960) will be different at depth, depending upon the pressure and other factors determined by the animal during a dive cycle. We did not test a variety of geometric configurations for partially collapsed air sinuses during this initial study, although this is planned for future studies.

Along all the bounding surfaces of the computational box, all three velocity components are prescribed as $v_x(t)=0$ and $v_z(t)=0$, and

$$v_y(y,t) = v_A[1 - \exp(-\Sigma t^2)]\sin(\gamma y - \varpi t),$$

where $\gamma = 2\pi f/c$ is the wave number; $c=1507\ \mathrm{ms}^{-1}$ is the sound speed in seawater at 15 °C; y is the left-to-right coordinate; ϖ is the angular frequency; $f=3500$ Hz is the frequency of the sound signal; $\Sigma = 6.1 \times 10^7\ \mathrm{s}^{-2}$ is a constant related to the signal ramp-up; $v_A = p_A/\rho c$ is the velocity amplitude of the plane wave generated by pressure with amplitude $p_A = 10^3$ Pa (corresponding to SPL of 180 dB re1 μPa). The initial conditions are consequently $\bar{v}(x)=0$, and $\bar{\sigma}(x)=0$. These initial and boundary conditions correspond to plane sound waves propagating in the left-to-right direction (transverse) with respect to the animal, with an exponential ramp up from a rest/unstressed state, up to full power within a fraction of a millisecond.

D. Material parameters

The material parameters needed for the isotropic constitutive equation described earlier are the density ρ, bulk modulus K, shear modulus G, and dynamic viscosity η. The sample density can be mapped from the CT image using a conversion from the Hounsfield units (Soldevilla *et al.*, 2005). Since the dynamic viscosity is not available as a map of the Hounsfield units, and needs to be estimated from the literature, we use the map proposed by Soldevilla *et al.* (2005) to assign representative "average" mechanical properties to tissues in the following groups: hard bone, soft bone, connective tissue, muscle, and acoustic fats/blubber.

To derive the stiffness moduli from the Young's modulus E as measured by Soldevilla *et al.* (2005), we compute the

TABLE I. Tissue parameters used for model.

Tissue type	Mass density ρ (kg m^{-3})	Bulk modulus K (MPa)	Shear modulus G (MPa)	Dynamic shear viscosity η (Pa s)
Hard bone	3000	2772	2083	900
Soft bone	2000	83	38	100
Connective	1075	2821	0.041	20
Muscle	1000	2102	0.033	20
Fats	950	1861	0.022	20

bulk modulus K from the speed of sound (connective tissue 1620 ms^{-1}, muscle 1456 ms^{-1}, and acoustic fats/blubber 1400 ms^{-1}) using

$$c_1 = \sqrt{\frac{K}{\rho}},$$

and further the Poisson's ratio ν from the formula

$$K = \frac{E}{3(1-2\nu)}.$$

So far, the viscosity values of these tissues have not been measured, and we employ values that are representative of the viscosities obtained experimentally for human [breast: $0.55 \leq \eta \leq 4.0$ Pa s; see Sinkus *et al.* (2005)], and bovine [biceps femoris: $3 \leq \eta \leq 17$ Pa s; Catheline *et al.* (2004)] tissues, and which are similar to the high content of high viscosity fats in the tissues of the odontocetes. It is noteworthy that this parameter is likely important and needs to be experimentally determined.

We assume Young's modulus and Poisson's ratio of $E=5$ GPa and $\nu=0.2$ for the hard bone, and $E=0.1$ GPa, and $\nu=0.3$ for the soft bone (because the specimen is a neonate, and the soft bone is mostly cartilaginous in a neonate mammal: These properties are estimates taken from Vincent, 1990). The damping in the bone has to be estimated from published data, in particular for human and bovine bones. The loss tangent for the bones in the kilohertz range is taken from Garner *et al.* (2000) as $\tan\delta \approx 0.01$, which gives the dynamic viscosity η using the approximate formula, $\eta \approx G\delta/2\pi f = E\delta/4(1+\nu)\pi f$, where f is taken as the forcing frequency.

For the ***tissues*** we obtain the set of parameters in Table I.

For the surrounding ***sea water*** we take: $\rho = 1000$ kg m^{-3}, $K=2102$ MPa, $G=0$ MPa, and $\eta = 2 \times 10^{-3}$ MPa s^{-1}, which corresponds to a strongly viscous Newtonian fluid. The high viscosity is used to damp out reflected and scattered waves. Note that the pressure waves generated by the motion of the boundary (i.e., the external forcing) are also being damped, but since these are the forced part of the motion of the water, the effect of damping is minor. The reflected and scattered waves have a strong shear component which is effectively damped by the high viscosity of the surrounding water.

The pterygoid sinuses are assumed to be filled with air at atmospheric pressure (sea level air pressure), hence of negligible stiffness (air is much more compressible than water), and consequently the interior of these cavities is not modeled. This is presumed not to introduce significant error, since the lowest resonant frequencies of cavities of this size are on the order of 100 Hz. Using a free-spherical air bubble model with a 10 cm radius and atmospheric pressure one obtains an underestimate of 33 Hz of the natural frequency, and various models correcting for additional stiffness are available, including a heuristic relationship for a whole-lung resonance of Cudahy *et al.* (1999) [refer to Finneran (2003) and references therein]. These resonant frequencies are significantly lower than our chosen forcing frequency of 3500 Hz.

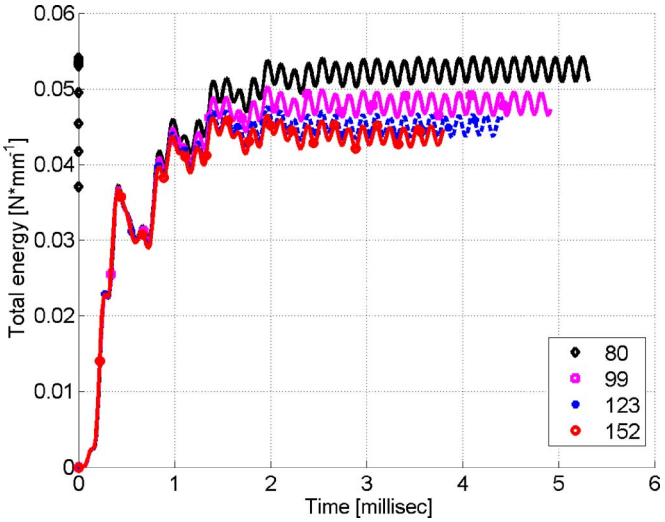

FIG. 3. Total energy in the computational box, including the surrounding water, as a function of time. The legend refers to the number of finite elements in the longitudinal direction N. The curves are ordered top to bottom as in the legend: the coarsest mesh $N=80$ is stiffer than the finest $N=152$.

For each resolution, the run was terminated when for a set number of cycles the total energy in the computational box oscillated around a constant value, indicating that a steady-state had been reached (hence at a different time instant for each resolution). A single processor personal computer (PC) with 2 GB of memory and a 3.4 GHz Pentium 4 CPU was used for these runs, with the longest run on the order of 40 CPU hours.

E. Results

The results of the simulations include the rate of steady-state energy dissipation at various spatial resolutions, maps of pressure distribution, heat distribution and dissipation, stress/strain regimes, and strain rates.

1. Total energy at steady state

The time variation of the total energy (potential plus kinetic) for the four mesh sizes used is shown in Fig. 3. Richardson's extrapolation (Roache, 1998) is used to estimate the convergent value of the total energy to assess the quality of the computed results. The normalized error in total energy may be defined as

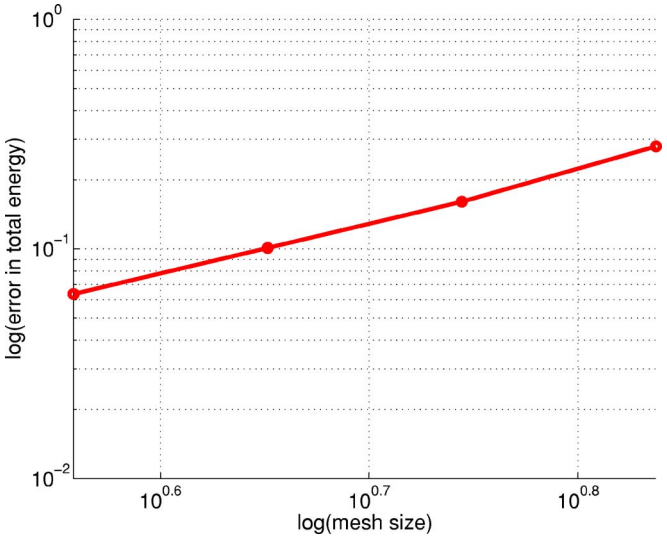

FIG. 4. The convergence plot for the total energy at steady state. Richardson extrapolation was used to estimate the converged total energy. The convergence rate is approximately 2.19.

$$e_h = \left| \frac{\Pi_R - \Pi_h}{\Pi_h} \right|$$

where Π_R is the estimated converged value; Π_h is the solution for mesh size h. The convergence graph is shown in Fig. 4, which indicates that the approximation error in the total energy is about 7% for the finest mesh. Clearly, accuracy in local quantities (as opposed to the global quantity—energy) is going to be lower. Therefore, more resolution (finer spatial mesh) is needed, and a transition to high-performance computer architectures (work in progress) would give us the ability to refine the computational meshes further, increasing accuracy in the results, including the bounds on the local quantities, for instance strain or dissipated energy density.

2. Pressure

Figure 5 shows the distribution of sound pressure for the finest mesh in a horizontal slice at the level of the sinuses and the ear bones (slice HA as shown in Fig. 2). The anatomic structures are displayed in color as surfaces for visualization purposes. Note that the highest pressure within the head, represented by a region of light gray pixels, is approximately 183 dB re: 1 μPa and is concentrated around the posterior aspect of the left ear (upper left region of Fig. 5). There is also a ridge of high pressure along the bottom of Fig. 5, which is the result of the acoustic stimulus planar wave entering the computational box from that side. In addition, there is a slight low-pressure depression around the posterior region of the right ear (Fig. 5). Note that the illustrations of pressure distribution are snapshots of a time-dependent process, where the maxima and minima at different locations are not synchronized.

The complex distribution of sound pressure is further illuminated in Fig. 6. It shows the pressure map at the same time instant as Fig. 5, but in transverse slices (perpendicular to the longitudinal axis of the animal), at various positions along the pterygoid sinuses (locations VA, VB, VC, and VD

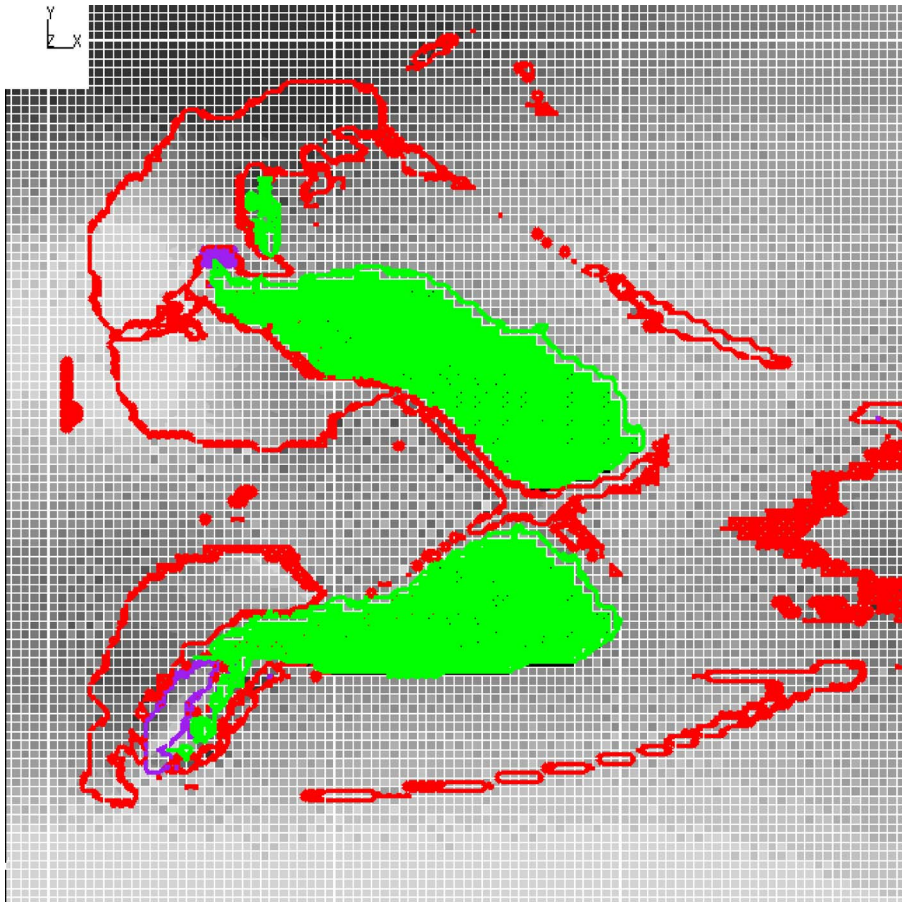

FIG. 5. (Color online) Pressure distribution for horizontal slice (HA) through the sinuses and the ear bones after the steady state has been reached. The left side of the animal is toward the top of the frame and the front of the animal is to the right of the frame. Light shade corresponds to positive pressure, dark shade corresponds to negative pressure, the pterygoid sinuses are shown in green, and the bony ear complexes in purple. The outlines of the skull bones are in red.

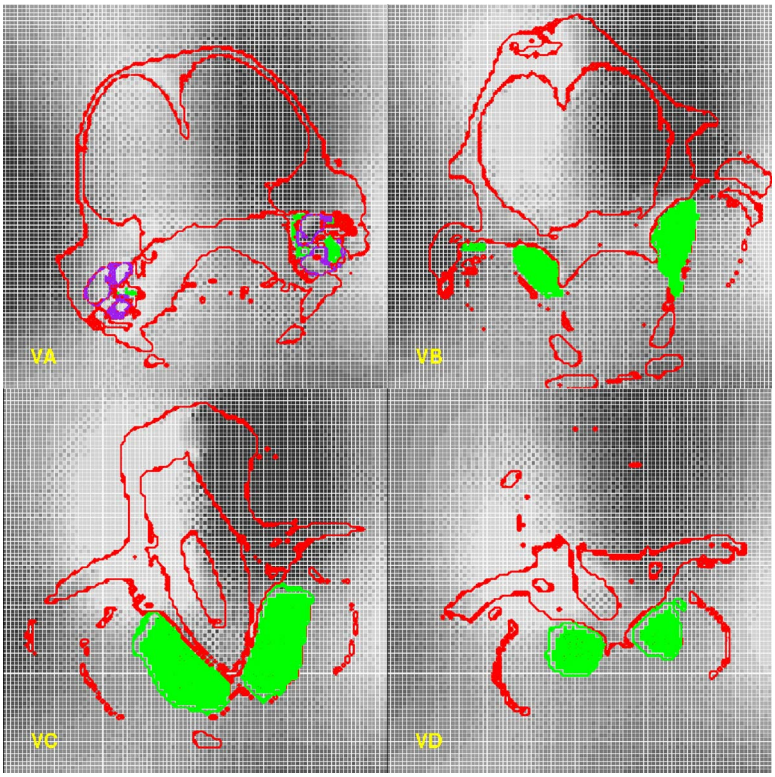

FIG. 6. (Color online) Pressure distribution at the same time as in Fig. 5. Vertical slices at different stations in the longitudinal direction along the sinus. (The locations of slices VA, VB, VC, and VD, are noted in Fig. 2. Light shade corresponds to positive pressure, dark shade corresponds to negative pressure, the pterygoid sinuses are shown in green, the bony ear complexes in purple, and the skull bones are outlined in red.

as shown in Fig. 2). The interaction of the sound pressure wave with the skull and other anatomical structures is clearly visible. For example, observe that the pressure generally varies more around the skull than in the soft tissues at the ventral side of the animal.

Note that at the frequency of 3500 Hz, the maximum pressure difference occurs within the space of the head. This can be seen as the darkest region on the right side of the head and the lightest region on the left side of the head (Fig. 6). To verify that this distribution of pressures is not just the "effect of the box," a simulation has been performed where the box was filled with seawater only. In this case, the distribution of pressures agreed with the prescribed motion (propagating planar wave). Consequently, we may conclude that the focusing of pressure is due to the presence of the tissues and not the dimensions of the box.

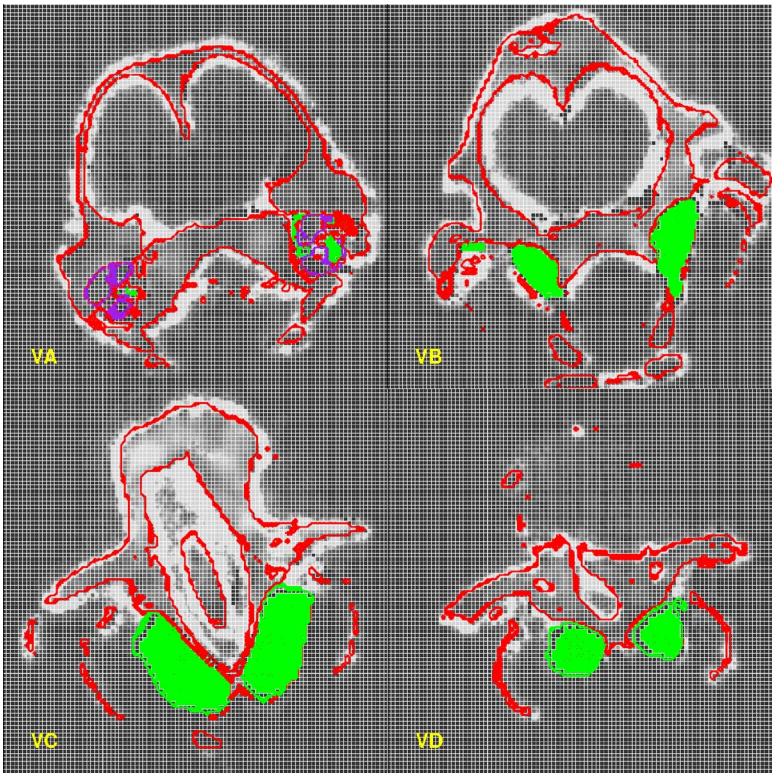

FIG. 7. (Color online) Energy dissipation density. Vertical slices at different stations in the longitudinal direction. (The location of each slice VA, VB, VC, and VD is shown in Fig. 2.) Light gray shades correspond to high density of energy dissipation, darker shade corresponds to lower density. The pterygoid sinuses are shown in green, the bony ear complexes in purple, and the skull bones are outlined in red.

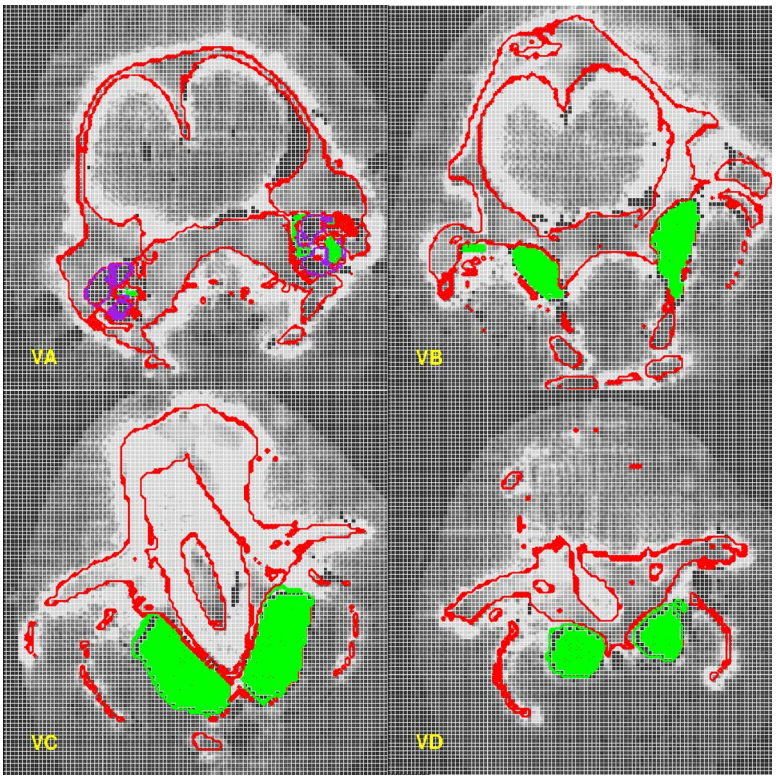

FIG. 8. (Color online) Maximum principal stretch displayed on vertical slices through the mesh. (The locations of the slices are displayed in Fig. 2.) High values (light shades) occur in the vicinity of the bone. Note that the distribution of the maximum principal stretch correlates with the distribution of the highest density energy dissipation. The pterygoid sinuses are shown in green, the bony ear complexes in purple, and the skull bones are outlined in red.

It also appears there is some "shielding" of acoustic pressure across the lower half of the head when compared to the upper half of the head, and appears as if it may be related to the presence of the pterygoid sinuses.

3. Local heating effects

It is known that the absorption of ultrasound at the bone/soft-tissue interface may lead to significant transient temperature rise (Myers, 2004). In the present case, the sound frequencies are much lower, but the mechanisms are similar: damping processes, primarily viscous, dissipate energy which is converted into heat. Therefore, as a first step one may look at the rate of energy dissipation to assess possible temperature increase as a result of local heating. Figure 7 illustrates the distribution of the dissipation energy density. Evidently, most of the energy is being dissipated in the soft tissue adjacent to the bone. In particular, it is interesting that the regions with the highest density of energy dissipation are within the brain at the edge of the braincase in VB of Fig. 7. In addition, panel VA of Fig. 7 shows a high-density region at the point where part of the brain (Vestibulo-cochlear nerve) passes through the internal auditory canal of the skull. This is the same region where a hemorrhage was found in a Blainville's beaked whale *Mesoplodon densirostris,* which stranded in association with naval sonar usage (NOAA, 2001).

These observations may also be correlated with the distribution of the *maximum principal stretch* (MPS). At any given point and time instant, the MPS is the largest of the stretches that the material experiences in any direction at that point. If we then consider the MPS for *all* points in the material, the greatest value is the quantity we refer to as the *largest* maximum principal stretch. Figure 8 demonstrates that the largest maximum principal stretch generally occurs next to the bones of the skull, including the mandibles.

The slope of the least-squares fit to the curves that express the time dependence of the largest local density of energy dissipation gives the maximum point wise *rate* of the dissipated energy density. An estimate of the maximum temperature rise rate can be estimated through the following expression (obtained from the linear heat conduction equation by neglecting heat diffusion and heat convection effects):

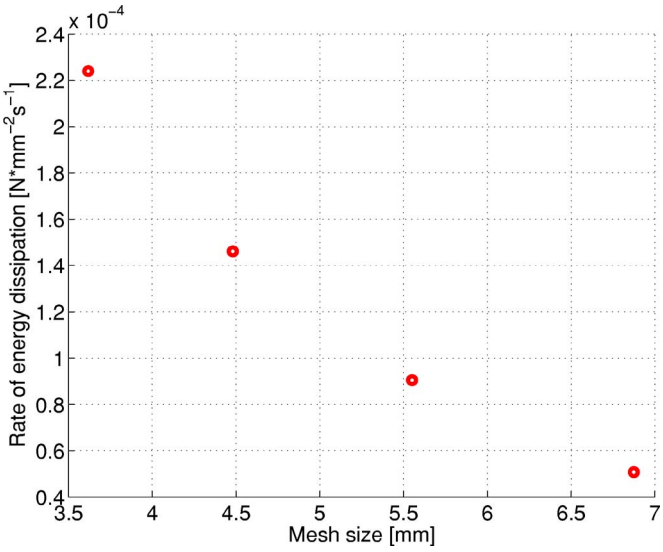

FIG. 9. Convergence of the local maximum of the point wise dissipated energy density. Finer meshes result in higher energy dissipation.

$$\dot{T} \approx \frac{\Phi_d}{\rho c_p},$$

where $\dot{T}$ is the rate of temperature increase; Φ_d is the density of the rate of dissipation; ρ is the mass density; and c_p is the specific heat at constant pressure. By reference to Fig. 9, we can estimate the maximum local rate of the density of energy dissipation as $\Phi_d \approx 4.0 \times 10^{-7}$ W mm^{-3}, which together with an estimate of the specific heat of soft tissues that is commonly used in the therapeutic ultrasound literature $c_p \approx 3500$ J kg^{-1} K^{-1}, and the mass density $\rho \approx 1000$ kg m^{-3}, yields the maximum local temperature increase rate $\dot{T} \approx 0.6 \times 10^{-4}$ K s^{-1}. Evidently, because heat diffusion and heat convection are being neglected this is an overestimate. Therefore, the temperature increase within the tissues due to sound excitation of expected exposure times on the order of 100 s appears to be a few millidegree Kelvin.

4. Injurious strains

The strain data is of lower accuracy than the energy data because strain results will depend strongly upon mesh size. We conjecture that there are no true stress singularities in the solution, and hence that the strain is finite everywhere. Consequently, the strain amplitudes should converge to finite values. However, for the strains the Richardson extrapolation is not available because our strain results are not in the asymptotic range yet, and may not be used to estimate converged values. To put the representation of the strains into context, consider that to begin to resolve the shear waves with speed of sound $c_s = \sqrt{G/\rho} \approx 5.7$ ms^{-1} (muscle), mesh resolution of approximately 0.4 mm would be required, whereas, the finest mesh size we used was 3.61 mm.

Nevertheless, since the response of the soft tissues at steady state is a mixture of dilatational modes and shear modes, some observations are possible based on the present range of resolutions (3.61–6.91 mm). Figure 8 illustrates the distribution of the *maximum principal stretch* at a particular time instant after the steady state has been reached. To quantify (see Fig. 10), the maximum principal stretch is approximately 1.5×10^{-4}.

IV. DISCUSSION

Our most important result is the success in combining CT scanning, tissue measurements, and finite element analysis tools to simulate the interactions between sound waves and anatomy. The innovation of combining these techniques has allowed us to ask questions that were not possible in previous studies (Aroyan *et al.*, 1992; Aroyan, 2001). For example, within the range of the physical parameters we tested, heating of the tissue and stretch (extensional strain) appear not to be factors that would lead to tissue damage in a neonate Cuvier's beaked whale. Although, wider ranges of the parameter values will need to be simulated to fully explore the possibility of injurious effects of these two factors. Another advancement from this work is the ability to pull CT data directly into the simulation software, with little or no need for data manipulation.

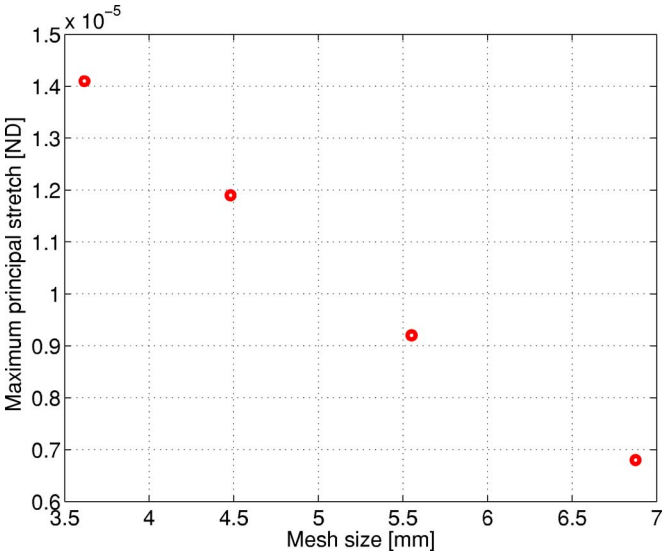

FIG. 10. Maximum point wise largest principal stretch during the steady-state vibration. Four different meshes.

At the intensity we tested (SPL=180 dB at 1 μPa), there is no indication of a significant deleterious effect on tissues from heating or strain. In ultrasound applications, a one minute exposure to ultrasonic frequencies can result in an increase of 6 °C, which is thought to have no deleterious effects on tissues (Hedrick *et al.*, 2005). In our case, the temperature increase due to a one minute exposure would probably amount to no more than a fraction of a degree Celsius. As such, temperature increase in tissue due to acoustic exposure is unlikely to be significant, with respect to possible injurious effects of strains alone, and within the acoustic parameters we tested and the restrictions noted above.

Biomechanics studies have established that injurious strains typically result when the stretch exceeds strains on the order of 10%. For instance, Sunderland (1978) published extensive work that show that nerve cells can typically sustain stretches of 20% while still functioning in an "elastic regime." The stretches in the present study (Fig. 8) are much lower, however, they are derived for a limited range of excitation parameters. If we extrapolate (under the assumption of linearity) from 180 to 220 dB re: 1 μPa, the pressure increases with a factor of 100. Correspondingly the strain amplitude may be expected to increase also with a factor of 100, placing the maximum stretch in the range of 1%. In addition, it is important to realize that at this point the strains produced in our model are not accurate owing to limitations in the mesh size, and we do not have a quantitative estimate of errors in strains. It is conceivable that our computed maximum stretches are in error, being underestimated.

One of the most interesting results of the simulations was the acoustic pressure distribution across the specimen. First, the maximum pressure differential is found within (across) the head in every transverse plane (perpendicular to the plane of the sound source) shown in Fig. 6. At this point in our investigation, we cannot determine whether these steep pressure gradients may have effects on sensory systems within the head. The dimensional extent of the maximum

differential pressure gradient is probably a function of the acoustic wavelength, which is related to the selected frequency (3500 Hz).

Another aspect of the simulated results of acoustic pressure distribution suggests that it might be possible to determine computationally whether a shielding or acoustic shadowing effect for the bottom half of the head exists. This might indicate a benefit if it confers protection from acoustic exposure to the hearing apparatus. With the present resolution it is possible to observe that the acoustic pressure varies more strongly at the top of the head, likely due to the presence of relatively stiff bones, but this issue deserves a more detailed examination.

V. CONCLUSIONS

The most promising outcome from this work is the broad spectrum of questions that can now be asked and answered. Prior to merging these techniques it was not possible to repeatedly query an anatomic system with questions of acoustic impact. At the given received level we tested (SPL=180 dB re: 1 μPa), there is no indication of a significant deleterious effect on the tissues. At the same time, neither can we determine what the simulations might reveal at higher intensities and/or different frequencies or mixtures of frequencies. However, the effect of a nonlinear dynamics upon the resonant vibrations has not been investigated. These are clearly interesting avenues for future investigations.

The effects of hydrostatic pressure on the geometry of air spaces, such as the pterygoids or peribullary sinuses, as described by Fraser and Purves (1960) will be different according to pressure and other factors determined by the animal during a dive cycle. With increasing hydrostatic pressure, the air within the sinuses may be systematically squeezed from the pterygoid sinuses to their respective peribullary sinuses. This is likely accomplished as blood fills the venous plexus and occludes the pterygoid sinuses as the air volume is compressed by the increased hydrostatic pressure with depth. We did not test a variety of geometric configurations for partially collapsed air sinuses during this initial study, but this is planned for future studies. As a consequence of the way we treat the internal sinuses as a special airspace (by assigning a unique Hounsfield value to the voxels corresponding to the sinuses), it may be possible to manipulate the size and shape of this internal cavity.

The source is lateral to the specimen in the example studied thus far. It would be interesting to investigate the effect of placing the source above or below the specimen, and how the acoustic shadowing and other parameters may change with frequency and intensity. It should be realized however that resonant vibrations of the tissues are excited by nonzero forcing irrespective of the direction of the oncoming sound wave. The resonant motion would not be generated only if the work-conjugate forcing identically vanished, which is statistically unlikely.

This specimen was CT scanned twice, once frozen and once thawed. Future studies should include a comparison of these data sets to understand the implications of the values that frozen tissue yields compared to thawed tissue. These two different conditions may help illuminate the implications of specimen geometry variations.

Increasing the resolution of the model significantly by uniform refinement (e.g., to finite element linear dimension of 0.5 mm) would improve the ability of the model to handle shear wave propagation. Likewise it would mean a substantial growth in the computational cost (computational grid of approximately 62 billion elements, compared to the 2.5 million elements used in this study). However, with adaptive, targeted refinement, the computational cost may be kept in check (Krysl *et al.*, 2003, 2004). A computational procedure of this nature is under development.

The treatment of the (semi-) infinite extent of the sea water environment is in this work only approximate. Use of infinite elements, coupling with boundary elements, and perfectly matched layers approximation are under consideration as alternatives.

It should also be noted that finite element simulation and analysis is an iterative process, beginning with a simplified model and moving to more complex objects and parameters with repeated iterations. This study represents the first step in a series. The anatomy and the range of parameters explored are necessarily simplified. So, these results can be understood as cracking the door open to reveal the most basic answers to the interaction between underwater sound and beaked whale anatomy. At the same time, the success of this first attempt encourages us to open the door more widely during successive iterations and sort through the cornucopia of remaining questions.

Numerical methods have been applied to simulate the effects of acoustic exposure in a complex biological system: the head of a neonate beaked whale *Ziphius cavirostris*. The presented approach offers promising prospects for future investigations for a variety of types of sounds and a variety of cetacean species.

ACKNOWLEDGMENTS

This work was supported by the U.S. Navy CNO-N45, with project management by Frank Stone and Ernie Young. The specimen of *Ziphius cavirostris* used in this study and in Soldevilla *et al.* (2005), was acquired with the help of Susan Chivers at the National Marine Fisheries Service (SWFC, San Diego) and is cataloged under the field number KXD0019.

Aroyan, J. L. (**2001**). "Three-dimensional modeling of hearing in *Delphinus delphis*," J. Acoust. Soc. Am. **110**(6), 3305–3318.

Aroyan, J. L., Cranford, T. W., Kent, J., and Norris, K. S. (**1992**). "Computer Modeling Of Acoustic Beam Formation In *Delphinus delphis*," J. Acoust. Soc. Am. **92**(5), 2539–2545.

Astley, R. J. (**2000**). "Infinite elements for wave problems: a review of current formulations and an assessment of accuracy," Int. J. Numer. Methods Eng. **49**, 951–976.

Balcomb, K. C. III and Claridge, D. E. (**2003**). "A mass stranding of cetaceans caused by naval sonar in the Bahamas," Bahamas J. Sci. **2**, 2–12.

Bayliss, A., Gunzberger, M., and Turkel, E. (**1982**). "Boundary conditions for the numerical solution of elliptic equations in exterior regions," SIAM J. Appl. Math. **42**, 430–450.

Brill, R. L., and Harder, P. J. (**1991**). "The effects of attenuating returning echolocation signals at the lower jaw of a dolphin *Tursiops truncatus*," J. Acoust. Soc. Am. **89**, 2851–2857.

Catheline, S., Gennisson, J. L., Delon, G., Fink, M., Sinkus, R., Abouelkaram, S., and Culioli, J. (**2004**). "Measurement of viscoelastic properties of homogeneous soft solid using transient elastography: An inverse problem approach," J. Acoust. Soc. Am. **116**(6), 3734–3741.

Cox, T. M., Ragen, T. J., Read, A. J., Vos, E., Baird, R. W., Balcomb, K., Barlow, J., Caldwell, J., Cranford, T., Crum, L., D'Amico, A., D'Spain, G., Fernández, A., Finneran, J., Gentry, R., Gerth, W., Gulland, F., Hildebrand, J., Houser, D., Hullar, T., Jepson, P. D., Ketten, D., MacLeod, C. D., Miller, P., Moore, S., Mountain, D., Palka, D., Ponganis, P., Rommel, S., Rowles, T., Taylor, B., Tyack, P., Wartzok, D., Gisiner, R., Mead, J., and Benner, L. (**2004**). "Understanding the Impacts of Anthropogenic Sound on Beaked Whales," J. Cetacean Res. Manage. **7**(3), 177–187

Cranford, T. W. (**1988**). "The anatomy of acoustic structures in the spinner dolphin forehead as shown by X-ray computed tomography and computer graphics," in: *Animal Sonar: Processes and Performance*, P. E. Nachtigall and P. W. B. Moore, eds., (Plenum, New York) pp. 67–77.

Cranford, T. W. and Amundin, M. E. (**2003**). "Biosonar Pulse Production in Odontocetes: The State of Our Knowledge," in *Echolocation in Bats and Dolphins*, J. A. Thomas, C. F. Moss, and M. Vater, eds. (The University of Chicago, Chicago) pp. 27–35.

Cranford, T. W., Amundin, M., and Norris, K. S. (**1996**). "Functional morphology and homology in the odontocete nasal complex: Implications for sound generation," J. Morphol. **228**, 223–285.

Cudahy, E. A., Hanson, E., and Fothergill, D. (**1999**). "Summary on the bioeffects of low-frequency waterborne sound," in Technical Report 3, Environmental impact statement for surveillance towed array Sensor system low-frequency active (SURTASS LFA) sonar.

Festa, G., and Vilotte, J. P. (**2005**). "The Newmark scheme as velocity-stress time-staggering: An efficient PML implementation for spectral element simulations of elastodynamics," Geophys. J. Int., **161**(3), 789–812.

Finneran, J. J. (**2003**). "Whole-lung resonance in a bottlenose dolphin (Tursiops truncatus) and white whale (Delphinapterus leucas)," J. Acoust. Soc. Am. **114**(1), 529–535.

Frantzis, A. (**1998**). "Does acoustic testing strand whales?," Nature (London) **329**, 29.

Fraser, F. C. and Purves, P. E. (**1960**). "Hearing in cetaceans: Evolution of the accessory air sacs and the structure and function of the outer and middle ear in recent cetaceans," Bulletin of the British Museum (Natural History) Zoology **8**, 1–140.

Garner, E., Lakes, R., Lee, T., Swan, C., and Brand, R. (**2000**). "Viscoelastic dissipation in compact bone: Implications for stress-induced fluid flow in bone," ASME J. Biomech. Eng., **122**(2), 166–172.

Hedrick, W. R., Hykes, D. L., and Starchman, D. E. (**2005**). *Ultrasound Physics and Instrumentation*, 4th ed. (Elsevier, New York).

Hildebrand, J. A. (**2005**). "Impacts of Anthropogenic Sound" in *Marine Mammal Research: Conservation beyond Crisis*, J. E. Reynolds *et al.*, eds. (The Johns Hopkins University Press, Baltimore, Maryland).

Hughes, T. J. R. (**2000**). *The Finite Element Method: Linear Static and Dynamic Finite Element Analysis* (Dover, New York).

Krysl, P., Grinspun, E., and Schroder, P. (**2003**). "Natural hierarchical refinement for finite element methods," Int. J. Numer. Methods Eng., **56**(8), 1109–1124.

Krysl, P., Trivedi, A., and Zhu, B. Z. (**2004**). "Object-oriented hierarchical mesh refinement with CHARMS," Int. J. Numer. Methods Eng., **60**(8), 1401–1424.

Myers, M. R. (**2004**). "Transient temperature rise due to ultrasound absorption at a bone/soft-tissue interface," J. Acoust. Soc. Am. **115**(6), 2887–2891.

NOAA (**2001**). "Joint Interim Report Bahamas Marine Mammal Stranding Event of 14-16" March 2000. Washington, D.C., US Department of Commerce and US Navy, available at: www.nmfs.noaa.gov/prof-res/overview/Interim-Bahamas-Report.pdf.

Norris, K. S. (**1964**). "Some problems of echolocation in cetaceans." in *Marine Bio-acoustics* W. N. Tavolga, ed (Pergamon Press, New York) pp. 317–336.

Řeřicha, P. (**1986**). "Optimum load time history for nonlinear-analysis using dynamic relaxation," Int. J. Numer. Methods Eng., **23**(12), 2313–2324.

Roache, P. J. (**1998**). *Verification and Validation in Computational Science and Engineering* (Hermosa Publishers, Albuquerque, New Mexico).

Rommel, S. A., Costidis, A. M., Fernandez, A. J. F., Jepson, P. D., Pabst, D. A., McLellan, W. A., Houser, D. S., Cranford, T. W., van Helden, A. L., Allen, D. M., and Barros, N. B. "Elements of beaked whale anatomy and diving physiology, and some hypothetical causes of sonar-related stranding," J. Cetacean Res. Manage., in press.

Rubin, M. B., and Bodner, S. R. (**2002**). ""A three-dimensional nonlinear model for dissipative response of soft tissue," Int. J. Solids Struct. **39**(19), 5081–5099.

Sinkus, R., Tanter, M., Xydeas, T., Catheline, S., Bercoff, J., and Fink, M. (**2005**). "Viscoelastic shear properties of in vivo breast lesions measured by MR elastography," Magn. Reson. Imaging **23**(2), 159–165 Sp. Iss. SI.

Soldevilla, M. S., McKenna, M. E., Wiggins, S. M., Shadwick, R. E., Cranford, T. W., and Hildebrand, J. A. (**2005**). "Cuvier's beaked whale (*Ziphius cavirostris*) head tissues: Physical properties and CT imaging," J. Exp. Biol., **208**(12), 2319–2332.

Sunderland, S. (**1978**). *Nerves and nerve injuries*, 2nd ed. (Churchill Livingstone, Edinburgh).

Vincent, J. F. V. (**1990**). *Structural Biomaterials* (Princeton University Press, Princeton, NJ).

Wagner, M., Gaul, L., and Dumont, N. A. (**2004**). "The hybrid boundary element method in structural acoustics," Z. Angew. Math. Mech. **84**, No. 12, 780–796.